ADVANCED ENERGY MATERIALS

Supporting Information

for *Adv. Energy Mater.,* DOI: 10.1002/aenm.202104076

Design Rules for Polymer Blends with High Thermoelectric Performance

*Osnat Zapata-Arteaga, Sara Marina, Guangzheng Zuo, Kai Xu, Bernhard Dörling, Luis Alberto Pérez, Juan Sebastián Reparaz, Jaime Martín, Martijn Kemerink, and Mariano Campoy-Quiles**

Supplementary information for

Design rules for polymer blends with high thermoelectric performance

Osnat Zapata-Arteaga[1], Sara Marina[2], Guangzheng Zuo[3], Kai Xu.[1], Bernhard Dörling[1], Luis Alberto Pérez[1], Juan Sebastián Reparaz[1], Jaime Martín[2,4,5], Martijn Kemerink[6,7], and Mariano Campoy-Quiles[1,]*

[1] Institute of Materials Science of Barcelona, ICMAB-CSIC, Campus UAB, CP 08193 Bellaterra, Spain.

[2] POLYMAT and University of the Basque Country, Av. de Tolosa 72, Donostia-San Sebastián, 20018, Spain.

[3] Institute for Physics and Astronomy, University of Potsdam, 14476 Potsdam-Golm, Germany

[4] Grupo de Polímeros, Centro de Investigacións Tecnolóxicas (CIT), Universidade da Coruña, Esteiro, 15471 Ferrol, Spain

[5] Ikerbasque, Basque Foundation for Science, 48013 Bilbao, Spain

[6] Centre for Advanced Materials, Heidelberg University, Im Neuenheimer Feld 225, 69120 Heidelberg, Germany.

[7] Division of Electronics and Photonic Materials, Department of Physics, Chemistry and Biology, Linköping University, Linköping, Sweden.

* Correspondence: Mariano Campoy-Quiles mcampoy@icmab.es, m.campoy@csic.es

Table of Contents

Thermoelectric properties for PBTTT:P3HT

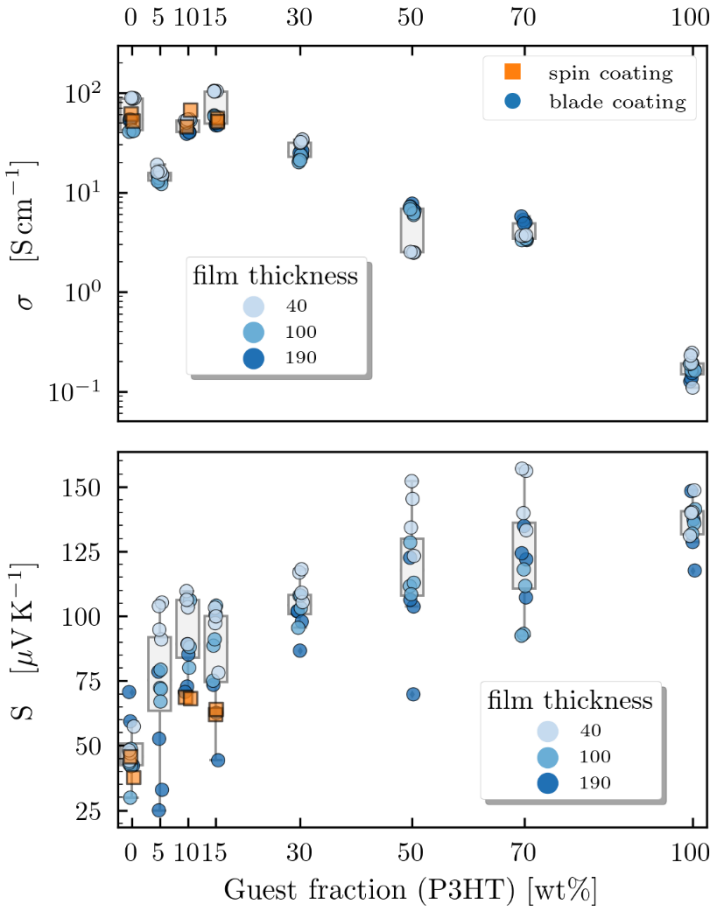

Figure S1**.** Thermoelectric properties for films of PBTTT with varied fractions of P3HT. Measurements correspond to different sections in the thickness gradient and processing methodology.

Figure S1 presents the thermoelectric properties of PBTTT with varied fractions of P3HT. We highlight that samples corresponding to spin-coated samples were fabricated from a different batch of PBTTT of a higher Mw (60-70 kDa) than the material used throughout the rest of the presented work (50 kDa).

Glass transition and HOMO levels of selected guest materials

Table 1**.** Literature-compiled T_g [°C], T_m [°C] and HOMO values for materials used in this work. The corresponding reference and characterization methods are also included. UV-Vis-NIR spectroscopy, rheology (Rh), differential scanning calorimetry (DSC), cyclic voltammetry (CV), ultraviolet photoelectron spectroscopy (UPS) and photoelectron yield spectroscopy (PYS). The values compiled in this table correspond to the reported T_g [°C], T_m [°C] of the backbone. The T_g marked with an * corresponds to a nearly 100% head-to-head configuration sample of PBTTT.

Polymer	T_g [°C]	T_m [°C]	HOMO [eV]
RR-P3HT	1, Rh[1]	248, DSC[2]	−4.7, PYS[3]
	12, Rh[4]	233, DSC[5]	−5.17, CV[6]
			−5.2, CV[7]
PBTTT	100, UV-Vis-Nir[8]	250, DSC[9]	−5.2, CV[10]
	106, Rh[1]	232, DSC[8]	−5.1, UPS[11]
	5*, Rh[1]		
PCDTBT	107, Rh[1]	277, DSC[12]	−5.5, CV[13]
	116, Rh[1]		−5.35, CV[13]
	119, Rh[1]		−5.42, CV[14]
	130, DSC[15]		
PCPDTBT	112, Rh[1]	318, DSC[16]	−5.9, CV[17]
	104, UV-Vis-Nir[8]		−5.68, CV[18]
PFO	71, Rh[1]	170, DSC[19]	−5.8, CV[20]
	70.8, Rh[1]		−5.8, CV[21]
PTB7-Th	40, Rh[1]	276, DSC[2]	−5.4, CV[22]
	60, Rh[23]		−5.3, CV[24]
	129, Rh[23]		−5.15, CV[25]
PBDB-T	100, DSC[26]	-	−5.33, CV[27]
PBDB-2F	-	-	−5.4, CV
PBDB-2Cl	-	-	−5.52, CV[28]
PC71BM	118, DSC[5]	-	−5.83, CV[29]
		-	−5.96, CV[30]
		-	−6, CV[31]

Summary for Table S1

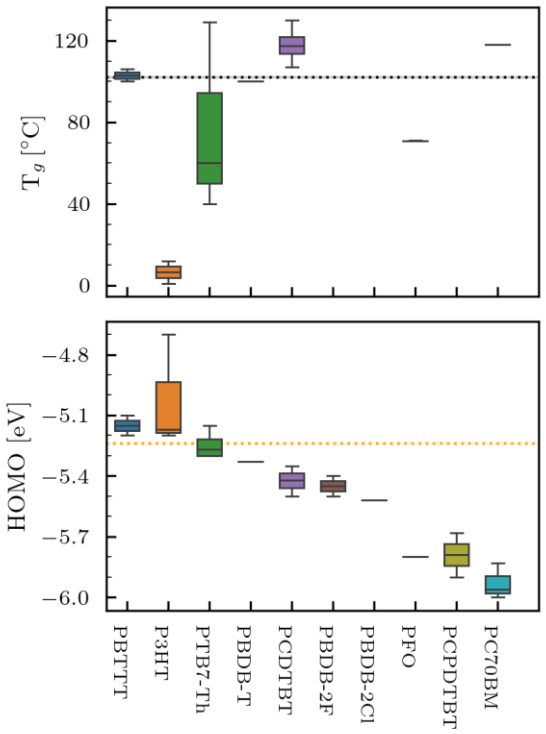

Figure S2**.** Summary plot for the glass transition temperature, and HOMO energy levels presented in Table S1

UV-Vis-NIR characterization

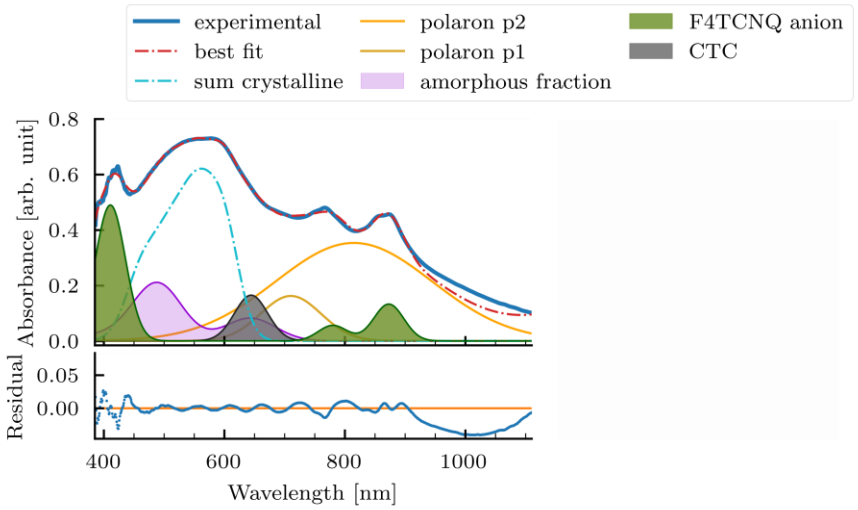

Figure S3**.** Example of the UV-Vis-NIR absorbance spectrum of a doped PBTTT sample. The spectral features were subjected to peak fitting and used for calculating the doping level.

To estimate the anion concentration, we deconvoluted the spectrum into several Gaussian contributions corresponding to the main species, i.e., neutral polymer, F4TCNQ•– anion, and polaron seen in Figure S3. For the fitting, we employed a least-square routine implemented in Python using the LMFIT library.[32] Then, the F4TCNQ anion concentration was estimated using the intensity of the anion and a molar extinction coefficient (50 000 mol^{-1} L cm^{-1} for F4TCNQ at 790 nm) along with Beer-Lambert's law.[33,34]

Structural and thermal analysis

AFM topography images

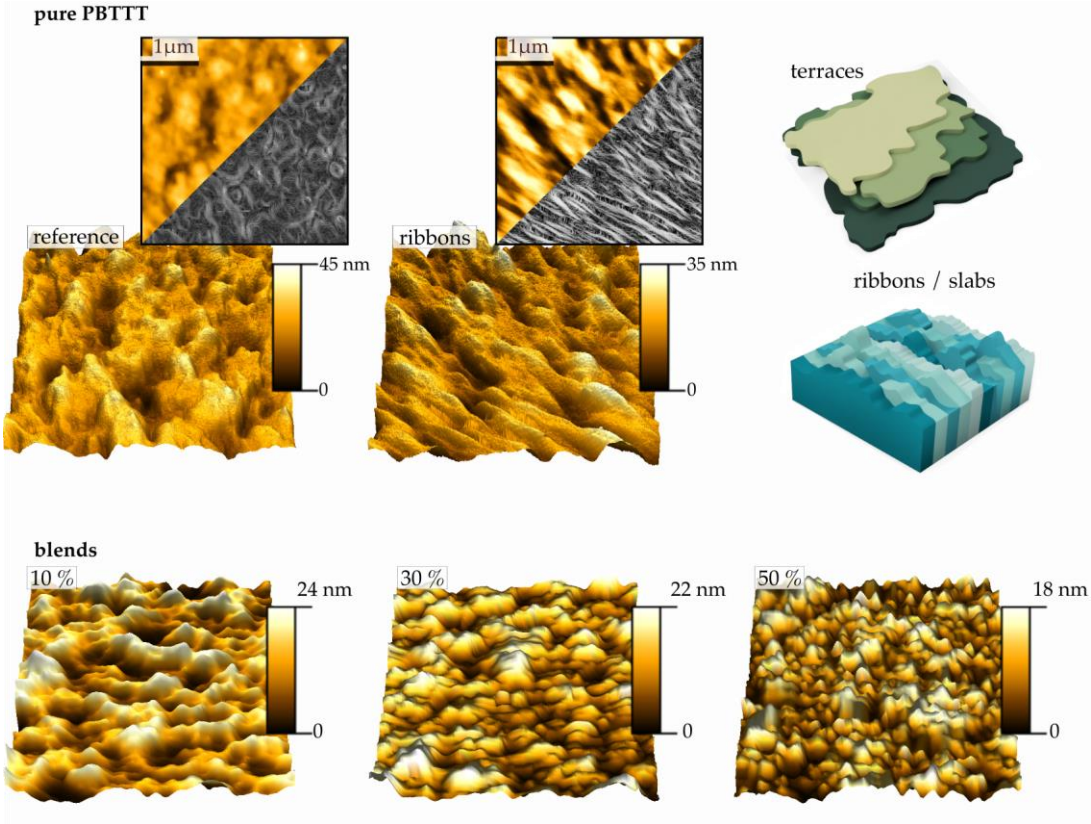

Figure S4**.** 3D Small area AFM topography images for the measurements shown in the main text. A 4 μm × 4 μm area is shown. For comparison, we include the topography of a pure PBTTT film with a typical ribbon structure. Insets in the reference and ribbon images show the 2D topography along the same image processed with a step edge filter (grayscale). An illustration of terrace and ribbon structures is also included for comparison.

FSC analysis

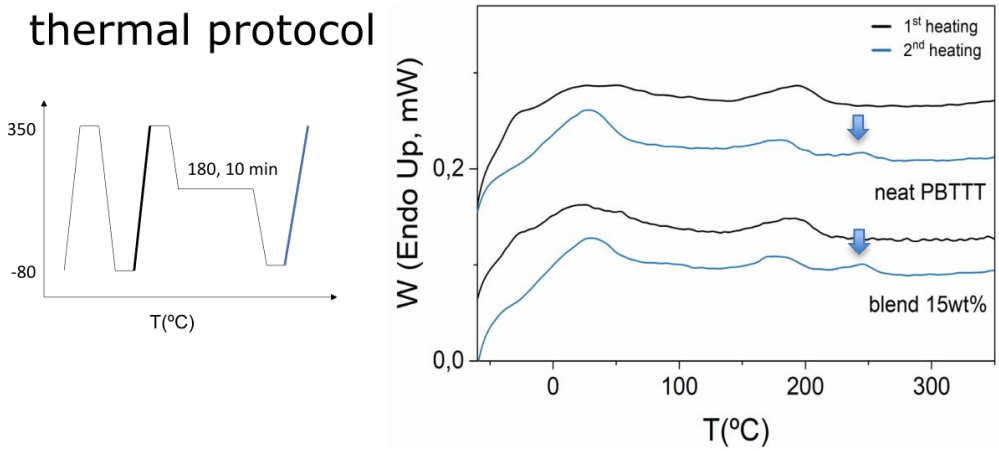

Figure S5. Thermal protocol employed (heating and cooling rate were 4000 ^{o}C s^{-1}) and FSC heating traces for neat PBTTT and a mixture of PBTTT:P3HT.

Figure S5 shows FSC measurements for undoped neat PBTTT and PBTTT with 15 wt % of P3HT. The heating traces of both neat PBTTT and PBTTT exhibit two endothermic peaks around 180 ^{o}C and 240 ^{o}C after being annealed at 180 ^{o}C. These peaks are associated with the melting of crystals and the terrace-to-ribbon transition of PBTTT, respectively. Clearly, the terrace-to-ribbon transition peak appears at the same temperatures in both samples, which rules out that blending with P3HT (with no dopant) shifts the transition towards lower temperatures.

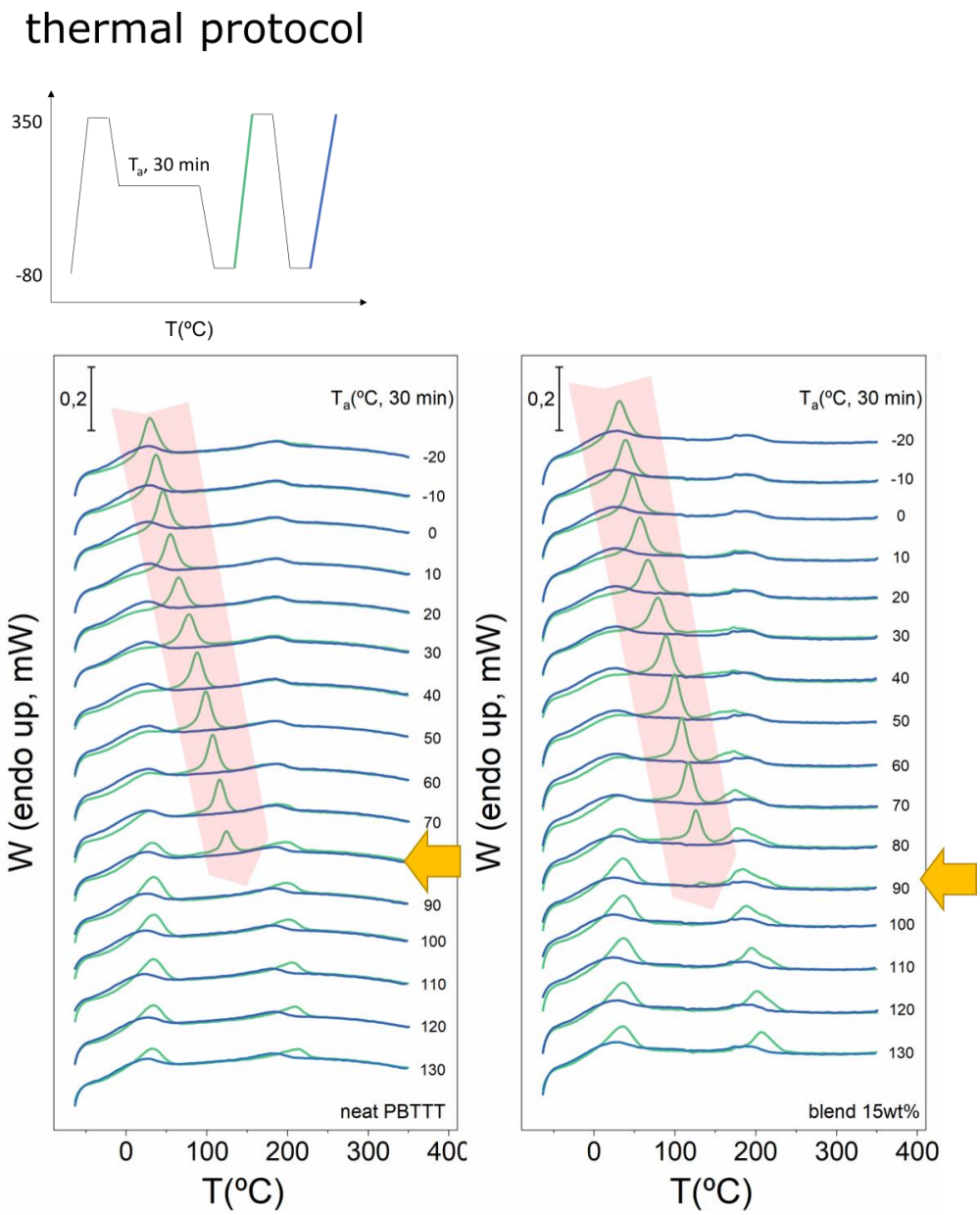

Figure S6. Thermal protocol and FSC measurements for neat PBTTT and a mixture of PBTTT:P3HT. Heating and cooling rate was 4000 ºC s^{-1}.

In order to figure out the glass transition temperature (Tg) of these materials, we conducted the a further FSC (thermal protocol employed is depicted in Fig S6. Bottom panel in Figure S6 show the results for undoped neat PBTTT and 15 wt% blend with P3HT. Curves shown correspond to the calorimetric heat flow rate signals recorded during the heating scans highlighted in the

thermal protocol schematic with equal colors. Annealing temperatures applied are shown on the right and side of curves.

The endothermic peaks associated with the physical ageing of the glass is shadowed in pink and thus indicates that at the annealing temperature applied, the system is in the glassy state. Conversely, if that peak does not show up, it means that the system is in the liquid state, hence above T_g. According to our data, the T_g of the neat PBTTT and of the blend (vitrified at 4000 ºC/s) are below 90 ºC and below 100 ºC, respectively. Therefore, for both materials, the annealing temperature applied for sample processing -180 ºC- is well-above the T_gs.

Interestingly, the endothermic peak related to the melt (ca 200 ºC) in the non annealed blend sample (blue curves) appears to consist in two shoulders, which can be related to the melt of each of the two materials (i.e., P3HT and PBTTT), with the bimodal shape becoming more apparent when annealing above the glass transition temperature. This, again suggests phase separation of the two materials.

AFM current maps

Figure S7 shows the 3D topography images with the current and mechanical measurements overlay. Here we highlight the presence of large agglomerates on the surface of the reference sample. These agglomerates are 700 nm high and 2 μm wide. Due to their lower electrical conductivity and increased hardness (indicated by larger values on the color scale) than the flat surface (cf. panel a and b), we ascribe them as neutral F4TCNQ accumulated during the vapor-

doping process. Interestingly, the films with added P3HT show fewer aggregates, even though all samples' doping conditions are identical. The latter may indicate that the polymer blends have a larger dopant uptake capacity than the reference material, as suggested by the UV-Vis-NIR analysis of doped species.

Additionally, the current AFM images show a good agreement with the macroscopic electrical measurements presented earlier. By adding 10 wt% of P3HT, the measured current values increases compared with the reference, indicating that the material becomes more conductive. Further addition of P3HT induces a gradual decay of the conductivity.

The mechanical measurements, excluding the agglomerates, show a narrow distribution of recorded values and a homogeneous color contrast in the flat surface. The latter can suggest that P3HT is well mixed within the PBTTT matrix, at least for the compositions studied. We also observe a stiffer character for PBTTT than P3HT, in good agreement with previous reports.[35] However, we highlight that the mechanical characterization is only qualitative, as we did not

measure a distinct reference material to correlate the measurement to an actual tensile strength value. As for polymer mixtures, we can only speculate they become stiffer than the neat starting material due to F4TCNQ infiltrating into the free volume of the polymer, reducing the segment motion and essentially vitrifying the material.[36]

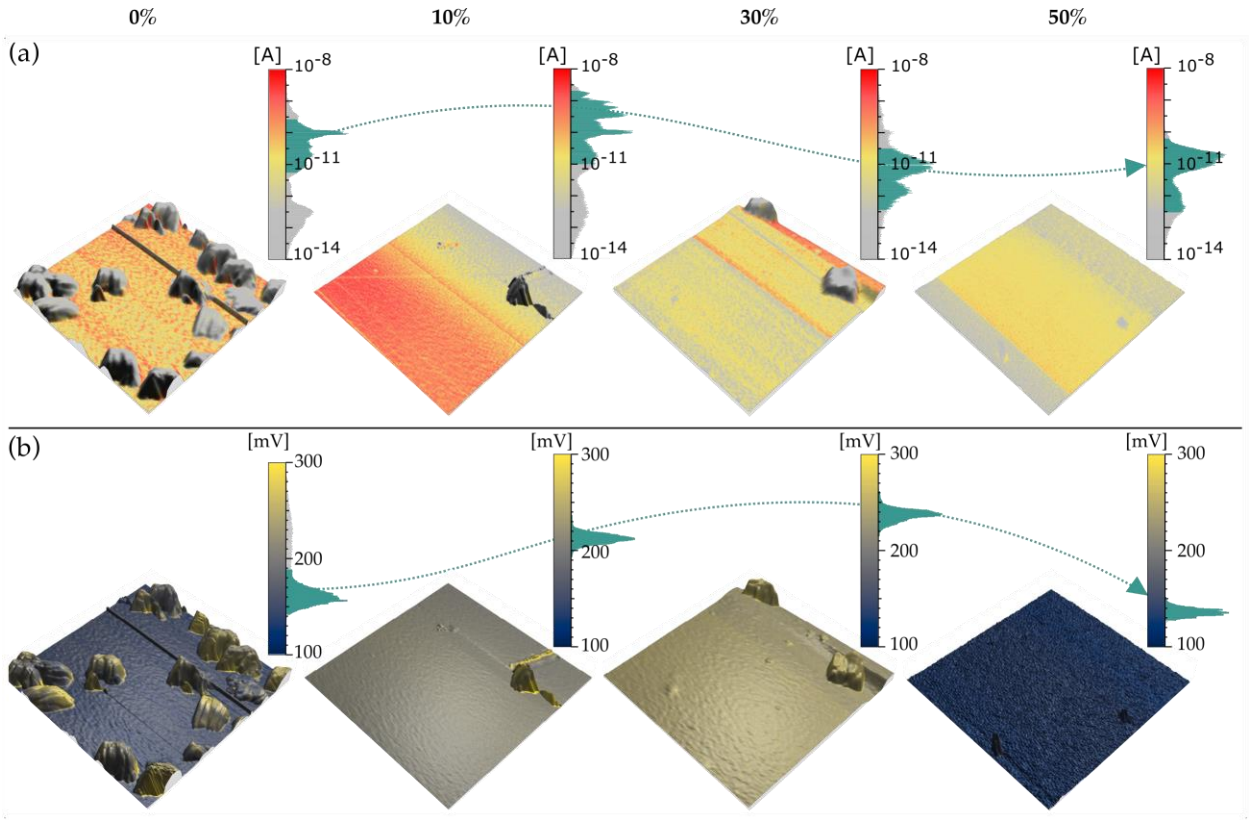

Figure S7**.** (a) Current and (b) mechanical AFM images overlaid on a 3D AFM topography map. The corresponding histograms are shown on the right side of the colorbar. Measured areas are 20 μm × 20 μm

GIWAXS patterns from blends of PBTTT:P3HT

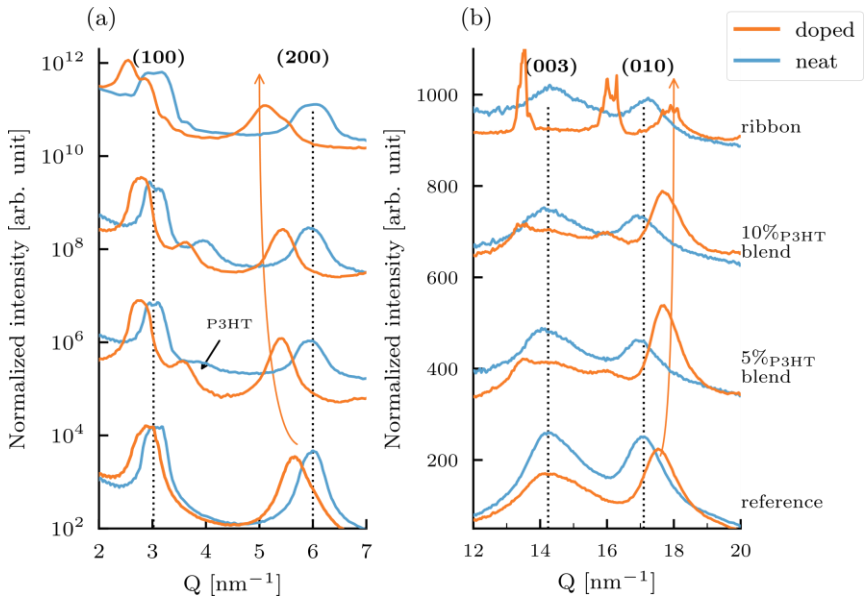

Figure S8**.** (a) Integrated out-of-plane and (b) in-plane GIWAXS patterns for the neat and doped films studied in the main section. Dashed lines indicate the position of prominent peaks of the neat-reference.

GIWAXS peak analysis

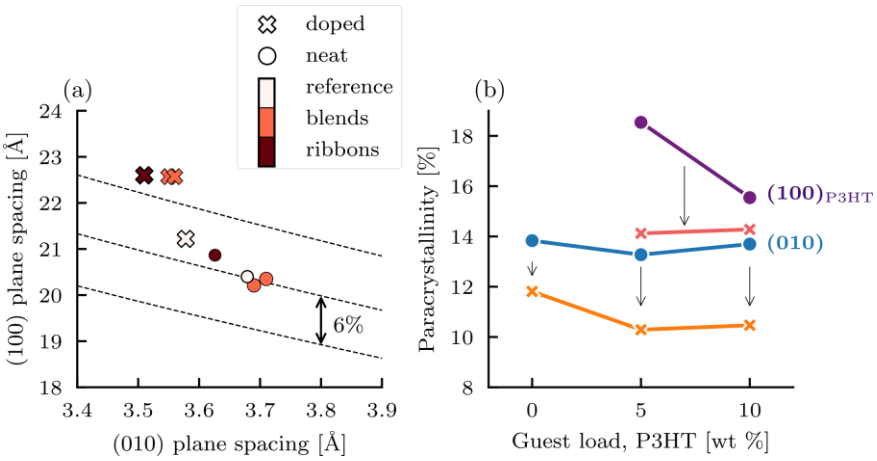

Figure S9**.** (a) Analysis for the (100) and (010) plane spacings obtained from 2D patterns. The dashed lines is a contour plot of the unit cell volume relative to a neat as-cast sample of PBTTT.(b) Paracrystallinity in the $\pi - \pi$-stacking (010) direction of PBTTT and for the lamellar direction in P3HT.

Raman characterization

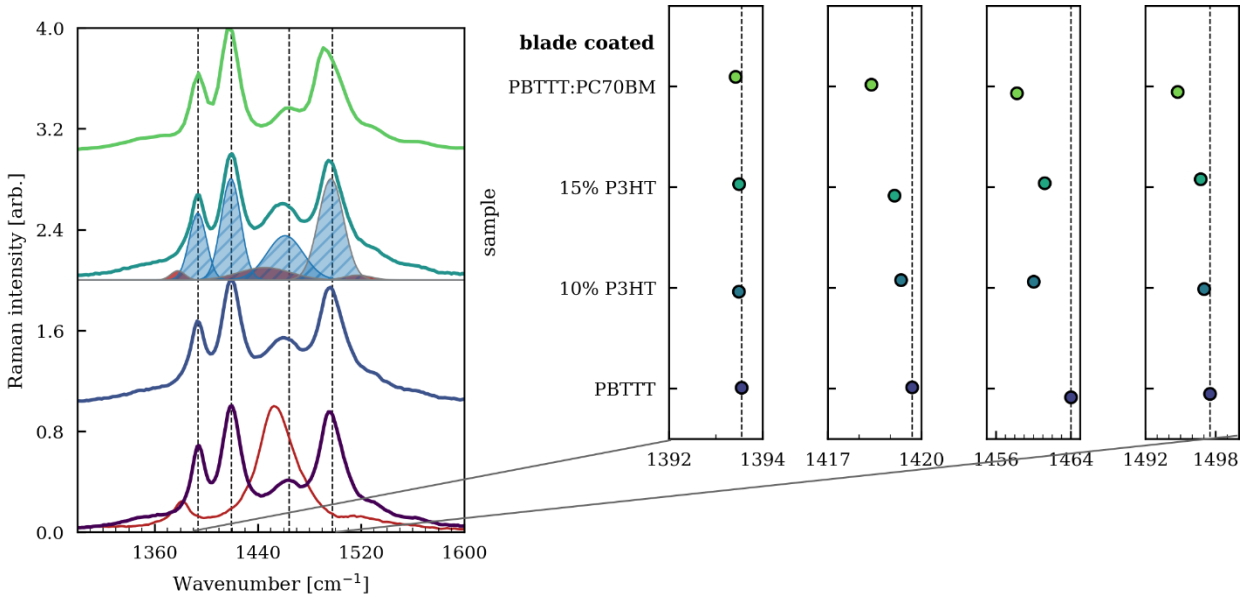

Figure S10. Resonant Raman spectra of selected samples. Measurements were done on doped blade coated samples at 488 nm. Also for comparison, we include the spectrum of PBTTT:PC70BM.

Thermoelectric properties, a comparison with literature data

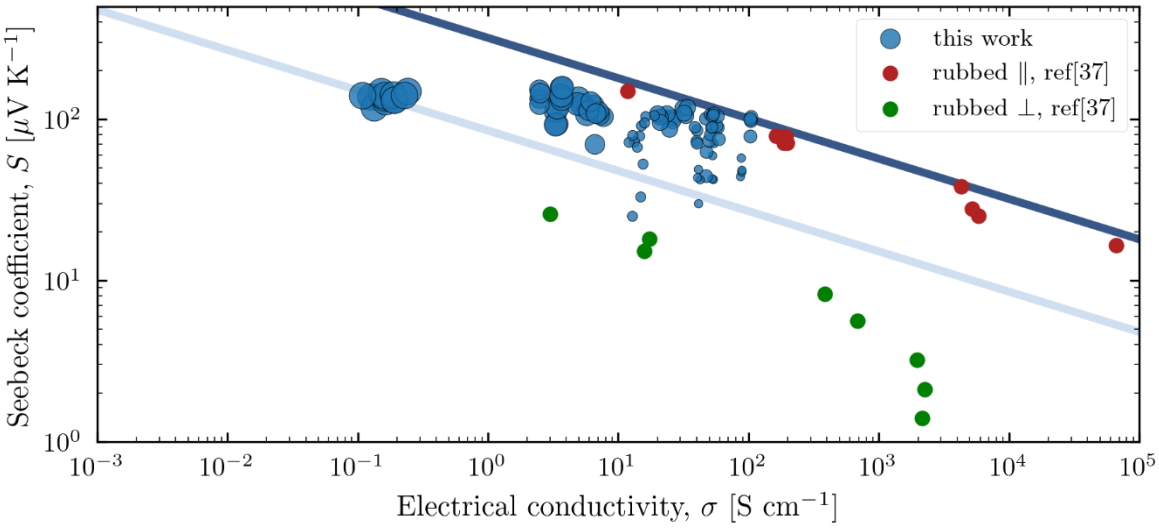

Figure S11**.** Seebeck coefficient as a function of the electrical conductivity. Blue circles correspond to the experimental data presented in the main text, and their size is related to the guest load ranging from 0 wt% to 100 wt%. Green and red circles correspond to literature data of rubbed PBTTT measured perpendicular and parallel to the rubbing direction.[37]

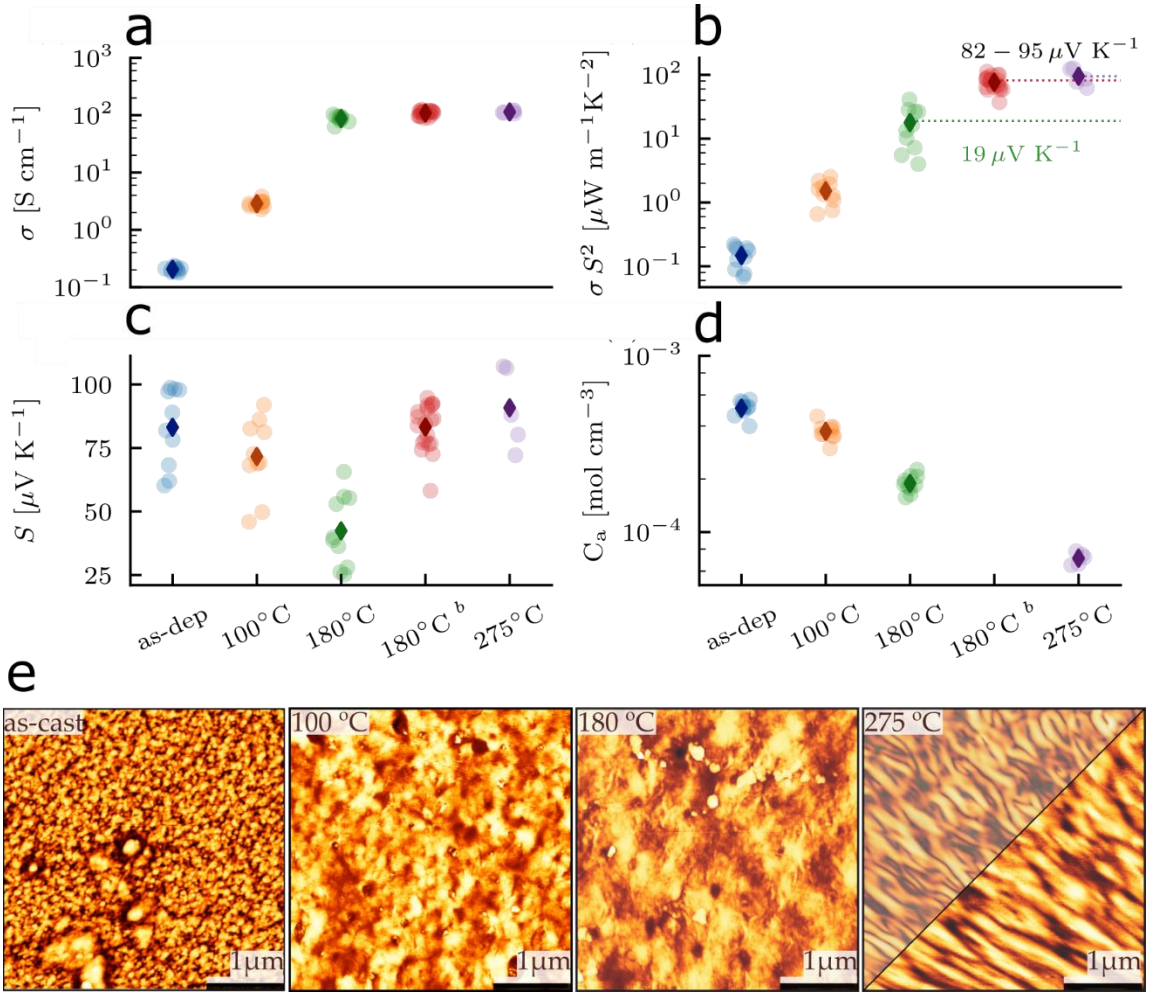

Figure S12**.** a-d. Thermoelectric properties of F4TCNQ-doped PBTTT annealed at different temperatures. For comparison, we also include the thermoelectric properties of a PBTT:P3HT blend, annealed at 180 ºC, marked as 180 ºC ^{b} (e) Shows the AFM for the corresponding samples.

Figure S12 shows the thermoelectric properties for F4TCNQ-doped pure PBTTT annealed at different temperatures. That is, as-cast, at 100 ºC, at 180 ºC, and at 275 ºC. All annealing procedures were done under nitrogen atmosphere and *before* doping. For comparison, we also include the thermoelectric properties of a PBTTT:P3HT (85 wt%/15 wt%) blend annealed also at 180 ºC. Their corresponding AFM topography images are shown in **Figure S12b.**

UV-Vis-NIR from blend of PBTTT:PTB7-Th

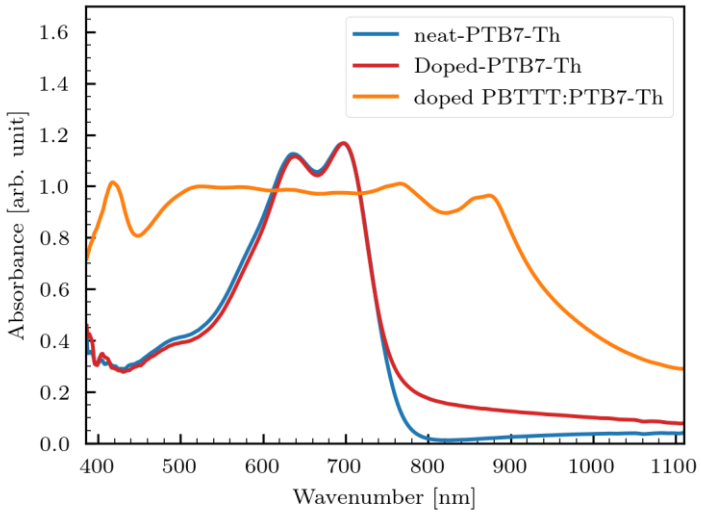

Figure S13. UV-Vis-NIR spectra of neat and doped PTB7-Th. Also doped spectra of the doped PBTTT:PTB7-Th film for guest fractions of 10 wt %

UV-Vis-NIR from blends of PBTTT:PBDB-derivatives

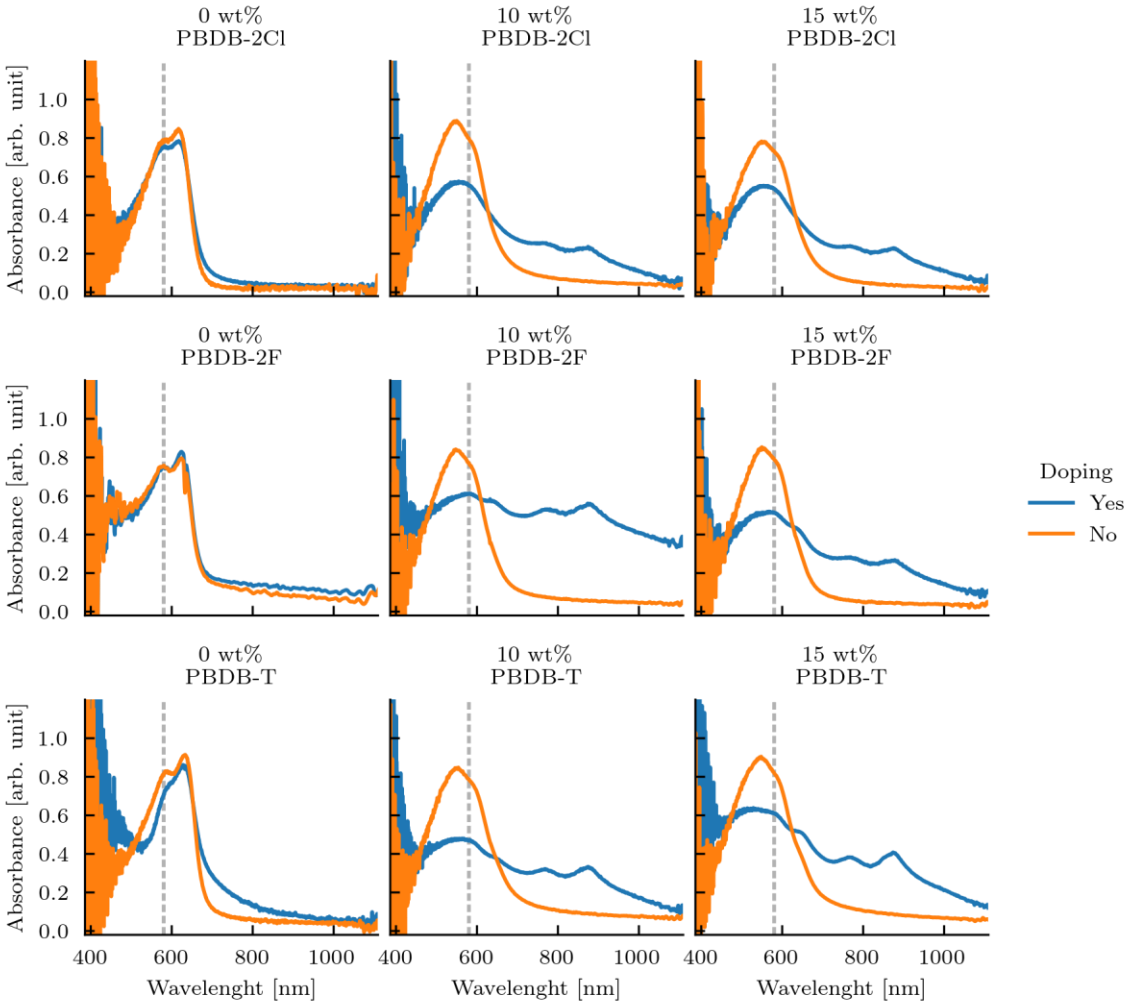

Figure S14. UV-Vis-NIR spectra of neat, and doped PBTTT:PBDB blends for guest loads of 10 and 15 wt % Dashed lines indicate the neutral band of guest material.

GIWAXS patterns for PBTTT:PFO, PBTTT:PTB7-Th

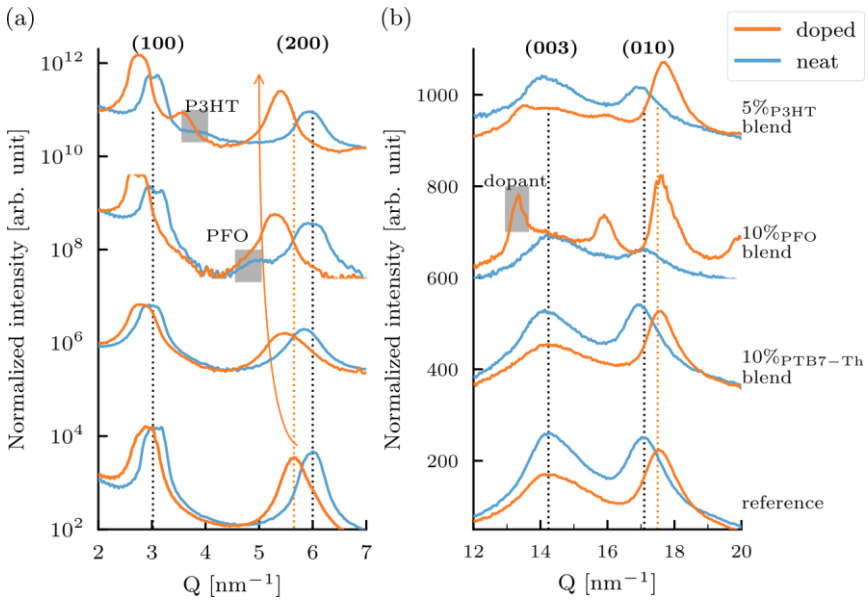

Figure S15. (a) Integrated out-of-plane and (b) in-plane GIWAXS patterns from the neat and doped films of PBTTT:PTB7-Th and PBTTT:PFO. Dashed lines indicate the position of prominent peaks of the neat reference. Gray squares indicate peaks that do not belong to PBTTT

Thermal conductivity characterization (FDTR)

Frequency-domain thermoreflectance characterization was done following a method described in the literature.[38] The experimental setup and representative examples of the characterization process are presented in Figure S16. The method uses two lasers to heat locally (pump, 405 nm) and probe (probe, 532 nm) the temperature at the surface of a sample. To enhance the thermal sensitivity of the method and limit the optical penetration depth, a 66 nm thick Au transducer was evaporated onto the surface of the samples. Both lasers were focused using an achromatic 30 mm focal distance lens to a spot size of $\sim 10\ \mu$m in diameter. The output power of the pump laser was modulated to a harmonic waveform in the frequency range between 1 kHz and 100 kHz, which generates thermally induced harmonic oscillations of the reflectivity of the sample, thus, leading to a modulation of the reflected power of the continuous wave probe laser. The quantity we focus on through this method is the phase lag between the pump heat wave

generated by the pump laser and the harmonic response of the sample as sensed by the probe laser using a lock-in amplifier. For the employed geometry, the frequency-dependent phase lag is modelled numerically, solving the parabolic heat equation. The thermal model used to fit the phase lag response curve describes the behavior of a stack of layers composed by the Au transducer, the studied film, the substrate, and an effective thermal boundary conductance that accounts for the two interfaces defined between the layers. The cross-plane thermal conductivity ($\kappa \perp$), the specific heat capacity (Cp) of the thin films, as well as the effective thermal boundary conductance (G) of the system were fitted using a least-squares routine.

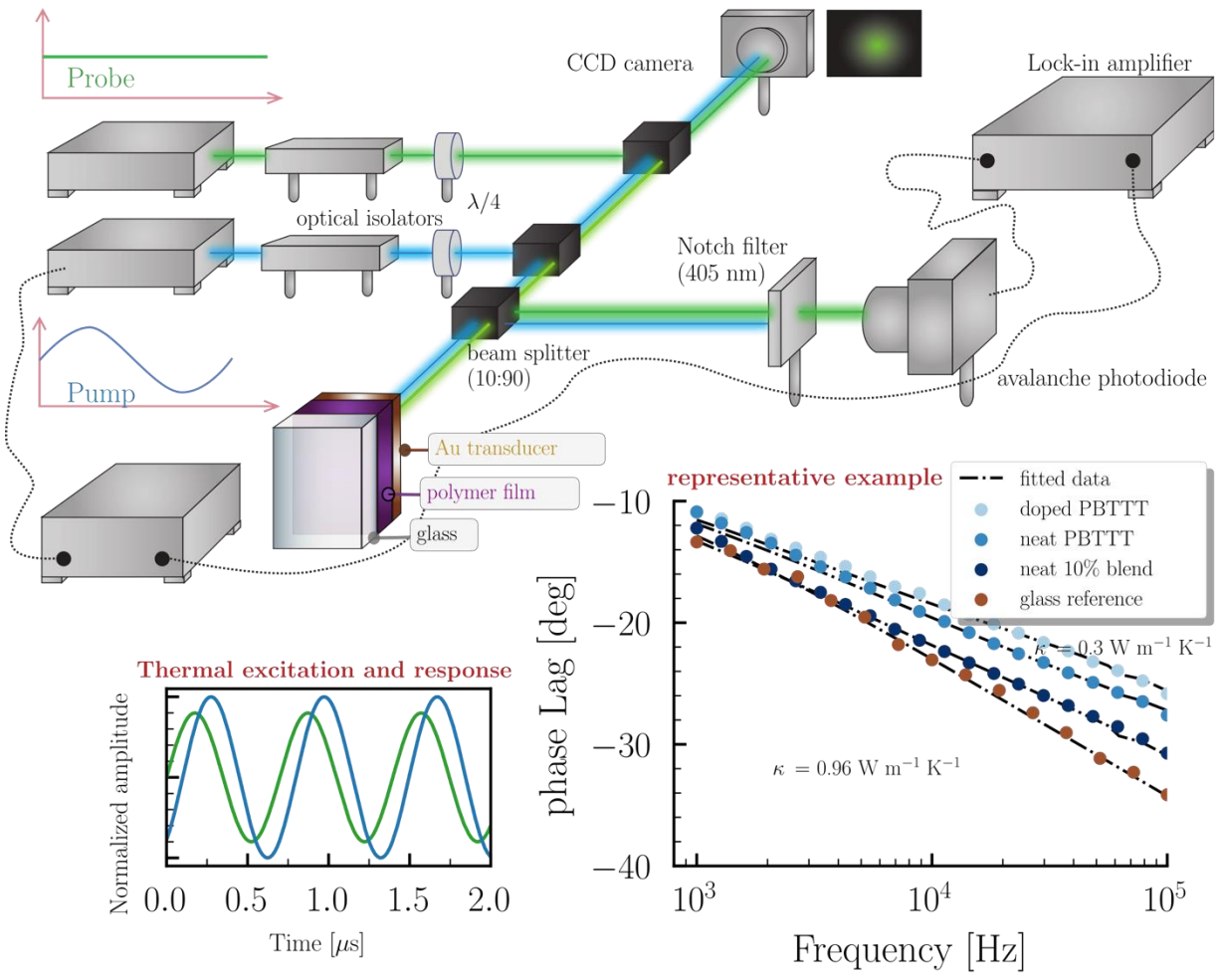

Figure S16. Experimental setup and representative examples of the characterization process in FDTR.

References

[1] R. Xie, A. R. Weisen, Y. Lee, M. A. Aplan, A. M. Fenton, A. E. Masucci, F. Kempe, M. Sommer, C. W. Pester, R. H. Colby, E. D. Gomez, *Nature Communications* **2020**, *11*, 893.

[2] M. Ghasemi, H. Hu, Z. Peng, J. J. Rech, I. Angunawela, J. H. Carpenter, S. J. Stuard, A. Wadsworth, I. McCulloch, W. You, H. Ade, *Joule* **2019**, *3*, 1328.

[3] Y. Wang, J. Chen, H. D. Kim, B. Wang, R. Iriguchi, H. Ohkita, *Frontiers in Energy Research* **2018**, *6*, 113.

[4] S. Wang, A. Mayer, K. Dhima, C. Steinberg, H.-C. Scheer, *Journal of Vacuum Science & Technology B, Nanotechnology and Microelectronics: Materials, Processing, Measurement, and Phenomena* **2013**, *31*, 06FB06.

[5] T. T. Ngo, D. N. Nguyen, V. T. Nguyen, *Advances in Natural Sciences: Nanoscience and Nanotechnology* **2012**, *3*, 045001.

[6] B. Burkhart, P. P. Khlyabich, B. C. Thompson, *Macromolecules* **2012**, *45*, 3740.

[7] J. Sun, M.-L. L. Yeh, B. J. Jung, B. Zhang, J. Feser, A. Majumdar, H. E. Katz, *Macromolecules* **2010**, *43*, 2897.

[8] S. E. Root, M. A. Alkhadra, D. Rodriquez, A. D. Printz, D. J. Lipomi, *Chemistry of Materials* **2017**, *29*, 2646.

[9] D. M. DeLongchamp, R. J. Kline, Y. Jung, D. S. Germack, E. K. Lin, A. J. Moad, L. J. Richter, M. F. Toney, M. Heeney, I. McCulloch, *ACS Nano* **2009**, *3*, 780.

[10] D. Kiefer, R. Kroon, A. I. Hofmann, H. Sun, X. Liu, A. Giovannitti, D. Stegerer, A. Cano, J. Hynynen, L. Yu, Y. Zhang, D. Nai, T. F. Harrelson, M. Sommer, A. J. Moulé, M. Kemerink, S. R. Marder, I. McCulloch, M. Fahlman, S. Fabiano, C. Müller, *Nature Materials* **2019**, *18*, 149.

[11] I. McCulloch, M. Heeney, C. Bailey, K. Genevicius, I. MacDonald, M. Shkunov, D. Sparrowe, S. Tierney, R. Wagner, W. Zhang, M. L. Chabinyc, R. J. Kline, M. D. McGehee, M. F. Toney, *Nature Materials* **2006**, *5*, 328.

[12] J. Maiz, M. Muñoz Rojo, B. Abad, A. A. Wilson, A. Nogales, D.-A. Borca-Tasciuc, T. Borca-Tasciuc, M. Martín-González, *RSC Advances* **2015**, *5*, 66687.

[13] N. Blouin, A. Michaud, M. Leclerc, *Advanced Materials* **2007**, *19*, 2295.

[14] H. Yi, S. Al-Faifi, A. Iraqi, D. C. Watters, J. Kingsley, D. G. Lidzey, *Journal of Materials Chemistry* **2011**, *21*, 13649.

[15] C. Müller, *Chemistry of Materials* **2015**, *27*, 2740.

[16] G. M. Fanta, P. Jarka, U. Szeluga, T. Tański, J. Y. Kim, *Polymers* **2020**, *12*, 1726.

[17] Y. Zhang, P. W. M. M. Blom, *Applied Physics Letters* **2011**, *98*, 143504.

[18] W. Dong, S. Xue, P. Lu, J. Deng, D. Zhao, C. Gu, Y. Ma, *Journal of Polymer Science Part A: Polymer Chemistry* **2011**, *49*, 4549.

[19] A. Perevedentsev, P. N. Stavrinou, P. Smith, D. D. C. C. Bradley, *Journal of Polymer Science Part B: Polymer Physics* **2015**, *53*, 1492.

[20] S. Janietz, D. D. C. Bradley, M. Grell, C. Giebeler, M. Inbasekaran, E. P. Woo, *Applied Physics Letters* **1998**, *73*, 2453.

[21] G. Lu, L. Bu, S. Li, X. Yang, *Advanced Materials* **2014**, *26*, 2359.

[22] C. Cui, W.-Y. Wong, Y. Li, *Energy Environ. Sci.* **2014**, *7*, 2276.

[23] J. Yin, W. Zhou, L. Zhang, Y. Xie, Z. Yu, J. Shao, W. Ma, J. Zeng, Y. Chen, *Macromolecular Rapid Communications* **2017**, *38*, 1700428.

[24] T. Jiang, J. Yang, Y. Tao, C. Fan, L. Xue, Z. Zhang, H. Li, Y. Li, W. Huang, *Polymer Chemistry* **2016**, *7*, 926.

[25] Q. Y. Li, J. Xiao, L. M. Tang, H. C. Wang, Z. Chen, Z. Yang, H. L. Yip, Y. X. Xu, *Organic Electronics* **2017**, *44*, 217.

[26] S. Brixi, O. A. Melville, N. T. Boileau, B. H. Lessard, *Journal of Materials Chemistry C* **2018**, *6*, 11972.

[27] Z. Fei, F. D. Eisner, X. Jiao, M. Azzouzi, J. A. Röhr, Y. Han, M. Shahid, A. S. R. Chesman, C. D. Easton, C. R. McNeill, T. D. Anthopoulos, J. Nelson, M. Heeney, *Advanced Materials* **2018**, *30*, 1705209.

[28] Q. Fan, Q. Zhu, Z. Xu, W. Su, J. Chen, J. Wu, X. Guo, W. Ma, M. Zhang, Y. Li, *Nano Energy* **2018**, *48*, 413.

[29] Z. Ding, X. Long, B. Meng, K. Bai, C. Dou, J. Liu, L. Wang, *Nano Energy* **2017**, *32*, 216.

[30] M.-A. Pan, T.-K. Lau, Y. Tang, Y.-C. Wu, T. Liu, K. Li, M.-C. Chen, X. Lu, W. Ma, C. Zhan, *Journal of Materials Chemistry A* **2019**, *7*, 20713.

[31] L. Lu, W. Chen, T. Xu, L. Yu, *Nature Communications* **2015**, *6*, 7327.

[32] M. Newville, T. Stensitzki, D. B. Allen, A. Ingargiola, **2014**.

[33] S. N. Patel, A. M. Glaudell, K. A. Peterson, E. M. Thomas, K. A. O'Hara, E. Lim, M. L. Chabinyc, *Science Advances* **2017**, *3*, e1700434.

[34] A. Hamidi-Sakr, L. Biniek, J.-L. L. Bantignies, D. Maurin, L. Herrmann, N. Leclerc, P. Lévêque, V. Vijayakumar, N. Zimmermann, M. Brinkmann, *Advanced Functional Materials* **2017**, *27*, 1700173.

[35] A. D. Printz, S. Savagatrup, D. Rodriquez, D. J. Lipomi, *Solar Energy Materials and Solar Cells* **2015**, *134*, 64.

[36] R. A. De Graaf, A. P. Karman, L. P. B. M. Janssen, *Starch/Staerke* **2003**, *55*, 80.

[37] V. Vijayakumar, Y. Zhong, V. Untilova, M. Bahri, L. Herrmann, L. Biniek, N. Leclerc, M. Brinkmann, *Advanced Energy Materials* **2019**, *9*, 1.

[38] A. Beardo, M. López-Suárez, L. A. Pérez, L. Sendra, M. I. Alonso, C. Melis, J. Bafaluy, J. Camacho, L. Colombo, R. Rurali, F. X. Alvarez, J. S. Reparaz, *Science Advances* **2021**, *7*, eabg4677.